

Supplemental Information

Variable Cell Growth Yields Reproducible Organ

Development through Spatiotemporal Averaging

Lilan Hong, Mathilde Dumond, Satoru Tsugawa, Aleksandra Sapala, Anne-Lise Routier-Kierzkowska, Yong Zhou, Catherine Chen, Annamaria Kiss, Mingyuan Zhu, Olivier Hamant, Richard S. Smith, Tamiki Komatsuzaki, Chun-Biu Li, Arezki Boudaoud, and Adrienne H.K. Roeder

Supplemental Information

Inventory

Figure S1 *vos1* mutants have increased variability in sepal size and shape, related to Figure 1.

Figure S2: A mechanical model of sepal morphogenesis predicts that spatiotemporal averaging of local variability in growth generates robust organ shapes, related to Figure 2.

Figure S3 Cell lineage tracking and cell area analysis on sepal epidermis, related to Figure 3.

Figure S4 Spatial variability of cell growth rates in area is decreased in maturing cells at the wild type-sepal tip, related to Figure 4.

Figure S5 *vos1* sepal and wild-type sepal tip show less temporal averaging of variability in the cell growth directions and greater stiffness, related to Figure 5.

Figure S6 *FtsH4* mutations increases ROS and leads to variable sepals, related to Figure 6.

Figure S7 *FtsH4* homolog YME1 affects growth rate and ROS production in yeast, related to Figure 6.

Supplemental Movie Legends

Supplemental Data File Legend

Supplemental Experiment Procedures

Supplemental References

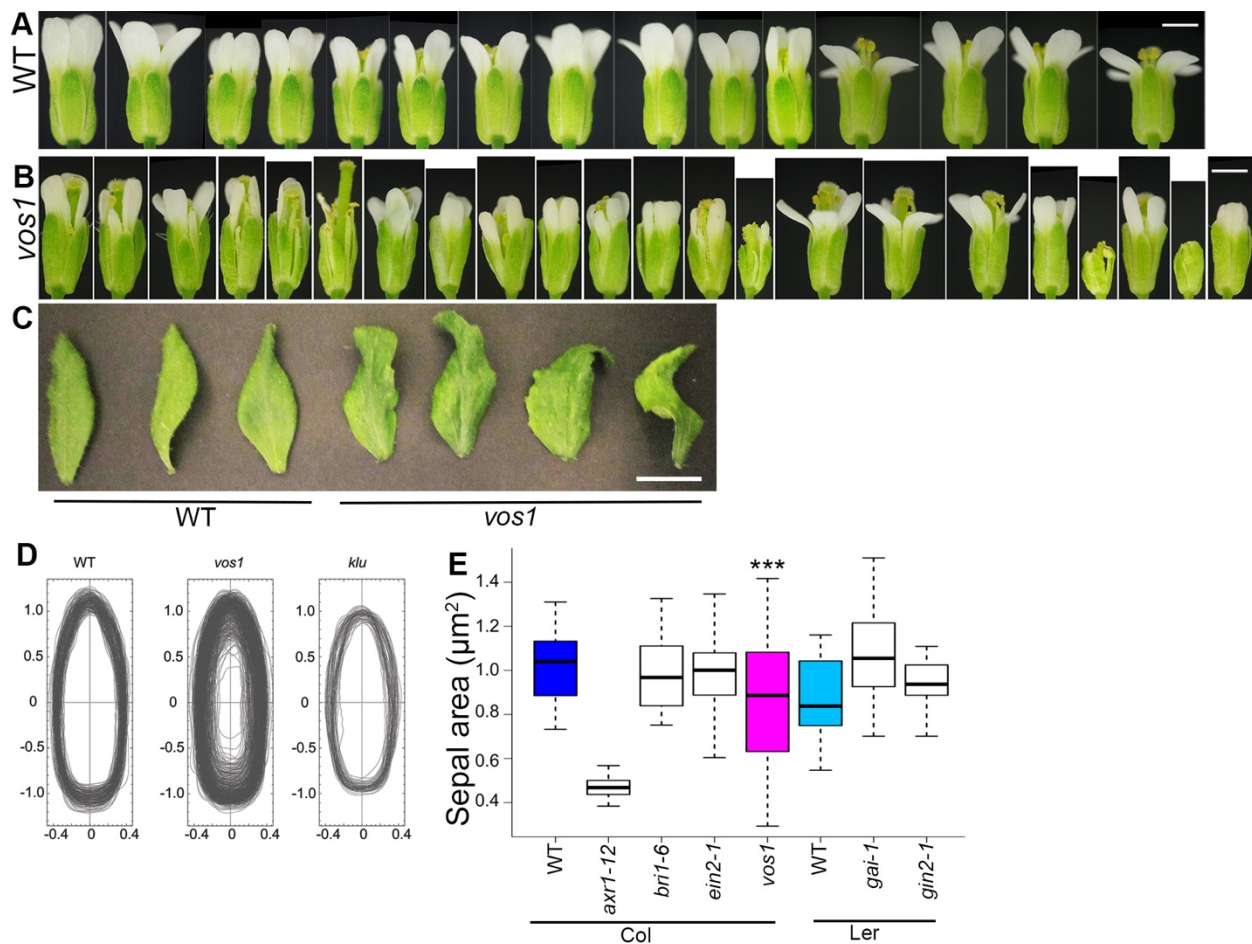


Figure S1 *vos1* mutants have increased variability in sepal size and shape, related to Figure 1.

(A) Flowers taken sequentially from the same WT inflorescence have similar sepals. (B) Flowers sequentially from the same *vos1* inflorescence have irregular sepal shape and size. Note that the *vos1* phenotype does not become progressively more irregular. (C) *vos1* mutants have more twisted cauline leaves than WT. (D) Outlines of WT, *vos1* and *klu* sepals revealing both size and shape variability (equivalent to Fig. 1E except that the sepals are not normalized by area). (E) Areas of mature stage 14 sepals from WT (blue and light blue), *vos1* (magenta; data reproduced from Fig. 1C for comparison) and hormone signaling mutants (white), showing that most mutants affecting organ size do not increase variance in area. *axr1-12*, *bri1-6* and *ein2-1* are in the Col (Columbia, blue) background. *gai-1* and *gin2-1* are in the Ler (Landsberg erecta, light blue) background. ***p < 0.001, significant difference in variance from WT (f test). In boxplots, the box extends from the lower to upper quartile values of the data, with a line at the median, and the whiskers extend past 1.5 of the interquartile range. Scale bars: 1 mm in A and B, 1 cm in C.

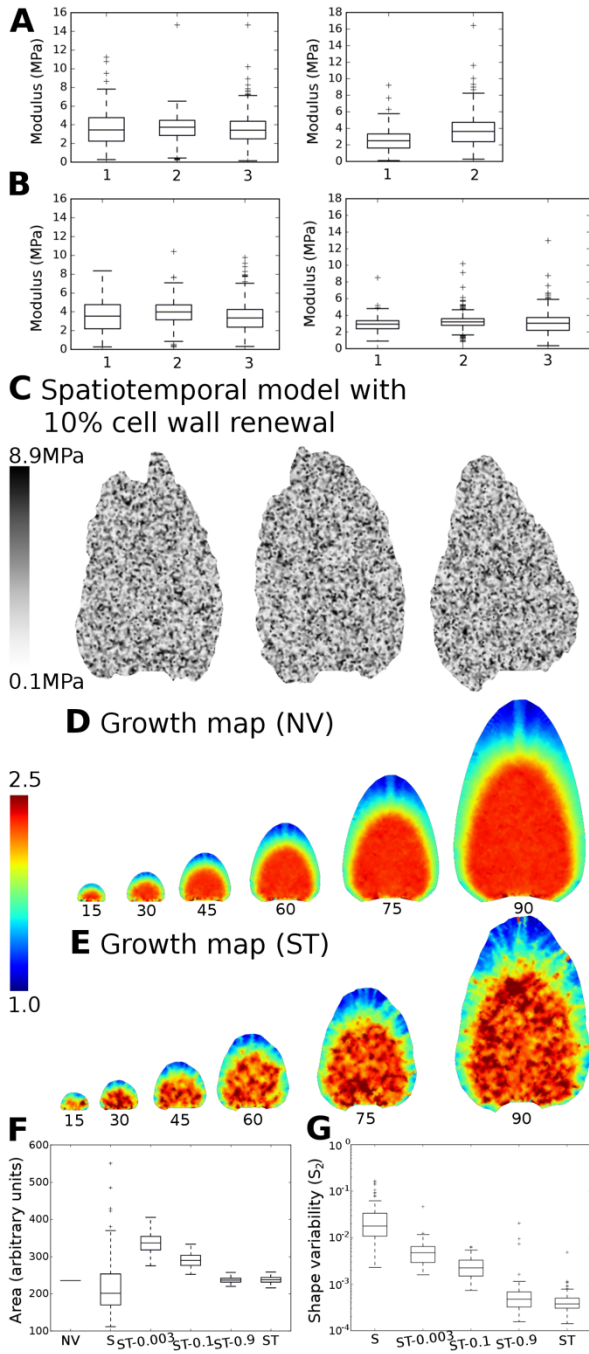


Figure S2: A mechanical model of sepal morphogenesis predicts that spatiotemporal averaging of local variability in growth generates robust organ shapes, related to Figure 2.

(A, B) Additional AFM measurements of wild-type (A) and *vos1* (B) sepals. Each box corresponds to one sepal and each plot to a separate batch of experiments

(C) Example of a model with intermediate temporal variability, in which mechanical properties are partially renewed: At each time point and at each vertex, mechanical properties are replaced by a weighted average of the properties at the previous step and of random properties following similar probability distribution functions. Here, the weight of the random modulus is 10% (ST-0.1) so that 90% of the previous properties are kept.

(D-E) Typical heat maps of the growth rates in simulations. Growth is computed every 15th step, as an integration of growth over the 15 previous steps.

(D) No variability model (NV).

(E) Spatiotemporal variability model (ST).

(F-G) Simulated sepal area (F) and shape (G) with the same models as in Figure 2K, with different levels of renewal: 0% (S), 0.3% (ST-0.003), 10% (ST-0.1), 90% (ST-0.9) and 100% (ST). For the final wild-type and mutant models (Figure 7) we chose 10% renewal. This amount of renewal allows the mechanical properties to be independent in about 10

computational steps, whereas the doubling time (i.e. the amount of time expected for the mechanical properties to be independent due to addition of cell wall material without cell wall remodeling) is observed to be 30 steps (for the values of pressure and mean modulus used here). Thus, 10% renewal is a reasonable value for temporal variability and simulation results are relatively insensitive to this choice.

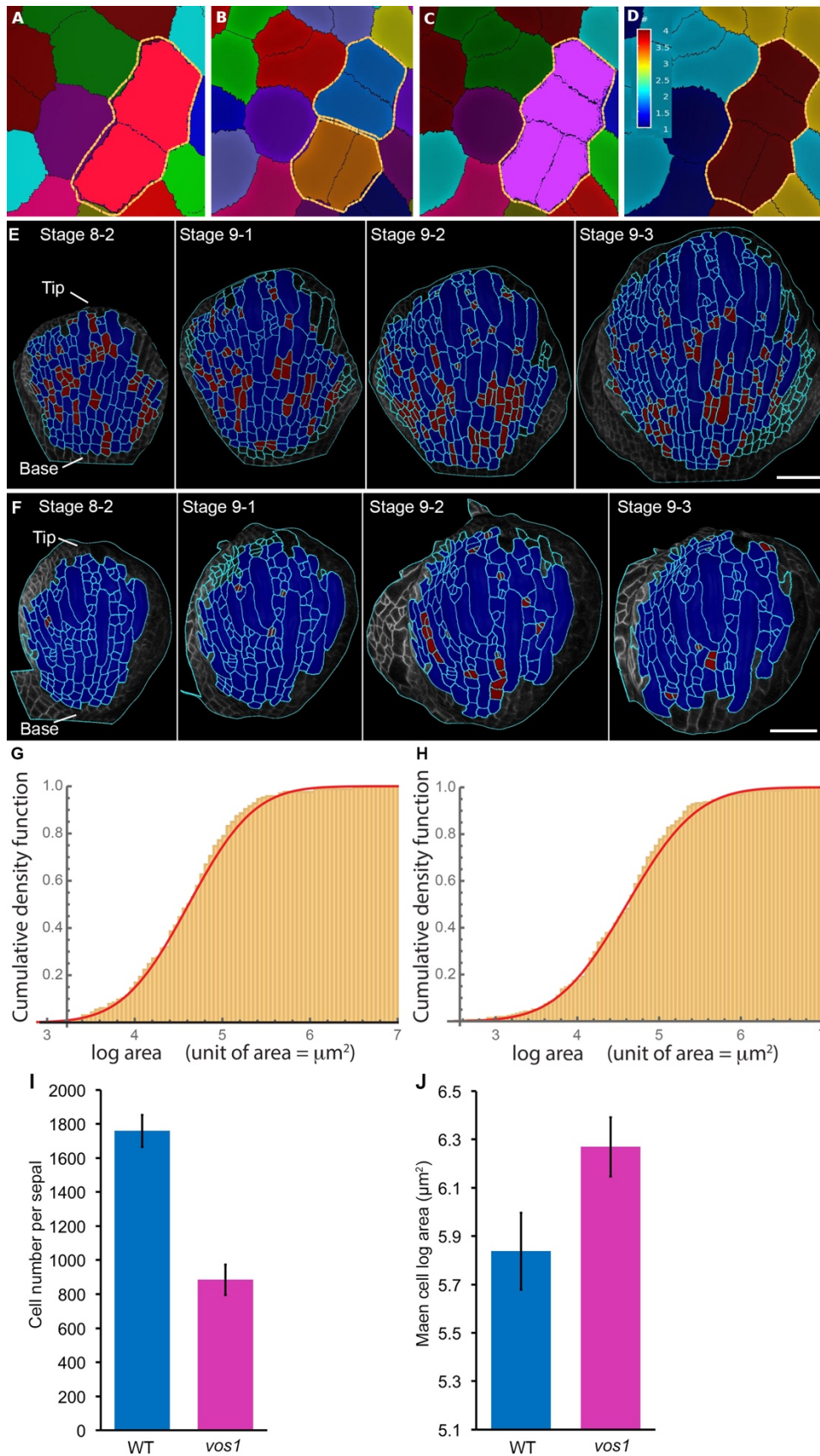


Figure S3 Cell lineage tracking and cell area analysis on sepal epidermis, related to Figure 3.

(A-D) The Multi Step Lineage Tracking (MSLT) tool tracks cell lineages over multiple consecutive time points (T0, T1, T2). Daughter cells of one cell have the same color and are marked with yellow line. (A) Cell lineage generated between T0 and T1, cells in red are daughters of a single cell at T0. (B) Lineage of the corresponding cells generated between T1 and T2. Both the upper cell and lower cell divide to make two daughter cells (blue, upper; brown, lower). (C) Using the MSLT it is possible to generate cell lineages between T0 and T2, showing that all 4 purple daughter cells in T2 descended from a single cell at T0. (D) Heat map of cell proliferation between T0 and T2. Color scale represents number of cells originating from one parent cell, i.e. brown color indicates 4 daughters at T2 descended from 1 cell at T0.

(E-F) Spatial maps of cell division in WT (E) and *vos1* (F) sepals. Flowers are staged based on their width. Each sub-stage lasts for 12 hours. The cells that have divided in the previous 12-hour sub-stage are marked in red. The WT sepal had active cell proliferation throughout the sepal at stage 8. Then the cells progressively exited from proliferation from the tip downward. *vos1* mutant sepals have low cell division rate throughout stages 8 and 9. Scale bars: 50 μ m in E and F.

(G-H) The logarithm of cell area in (G) WT and (H) *vos1* sepals at stage 8-1 follows normal distribution (red lines show the normal distribution fit). $n = 166$ in E, and 220 in F. This allows us to analyze the average logarithm of cell area.

(I) Total number of cells in mature WT and *vos1* sepals (stage 13).

(J) Average of the logarithm of cell area for WT and *vos1* sepals at stage 13. Mature *vos1* sepals have fewer cells while with larger cell area. $n= 4$ biological repeats for each genotypes in I and J, mean \pm SD.

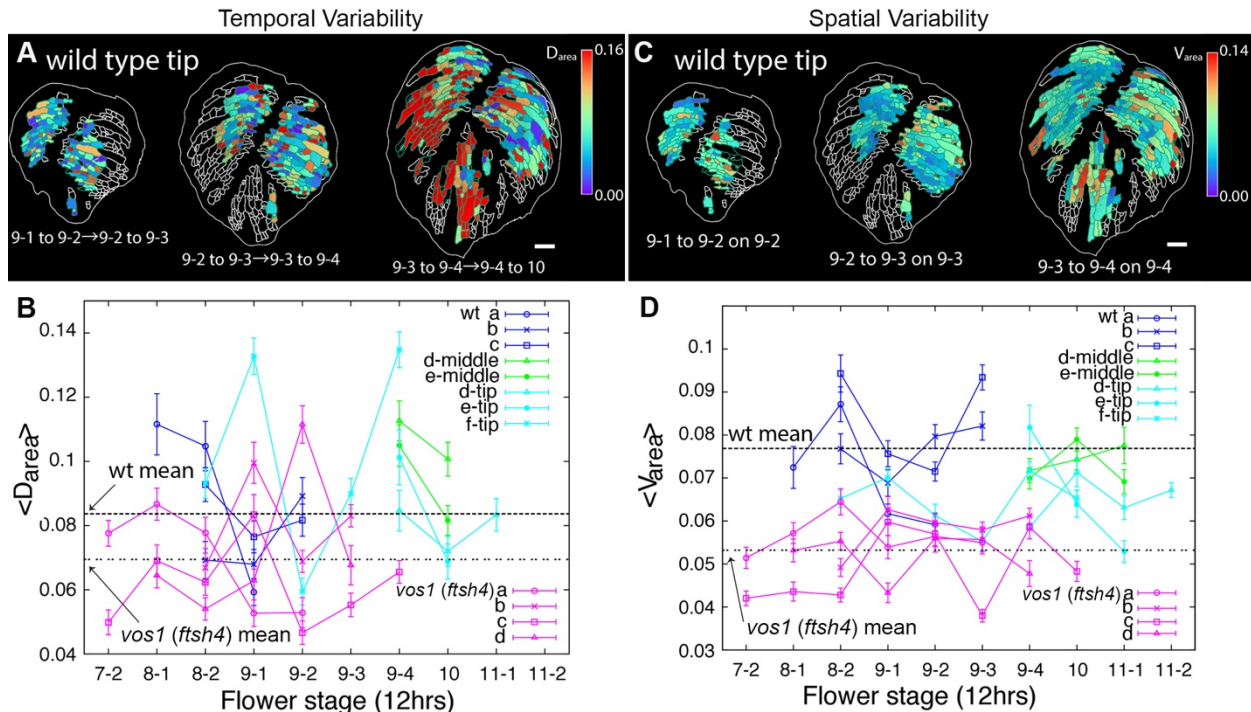


Figure S4 Spatial variability of cell growth rates in area is decreased in maturing cells at the wild type-sepal tip, related to Figure 4.

(A) Temporal variation of the cell growth rate in area (D_{area} , see materials and methods for details) of the tip part of a wild-type sepal, where the cells are maturing. The images were taken such that the top of the flower is shown revealing the tips of three sepals. In comparison flowers in Fig. 4 were imaged from the side. Variability is displayed as a heat map with high variability in red and low variability in blue. Consecutive 12-hour growth intervals are analyzed; for example, 8-1 to 8-2 → 8-2 to 9-1 means that the growth rate during the 12-hour interval from stage 8-1 to 8-2 is compared to growth rate during the 12-hour interval from stage 8-2 to stage 9-1.

(B) Graph plotting the average temporal variability of the areal growth rates ($\langle D_{\text{area}} \rangle$ = the average of D_{area}) in each sepal epidermis. The $\langle D_{\text{area}} \rangle$ plots from Fig. 4C are reproduced here (wild type a-c and *vos1* a-d), for comparison to the wild-type tip data. We divide the sepals of two wild-type flowers imaged at relative later stages (flower d and e) into the middle and tip (defined based on the differentiation of stomata). Wild-type flower f is the flower shown in A and only the tip is available for analysis. Note that for all flowers, the average temporal variability $\langle D_{\text{area}} \rangle$ plots largely overlap suggesting there is little difference between the middle and the tip parts of the wild-type sepals.

(C) Local spatial variation in the cell growth rate in area is decreased in the tip of a wild-type sepal. Local spatial variability is quantified by calculating the differences in growth rates for a cell and all of its neighbors (V_{area}) in the tip of wild type sepals for each 12-hour interval of growth (see Experimental Procedures for details). Variability is displayed as a heat map with high variability in red and low variability in blue.

(D) Graph plotting the average spatial variability in areal growth rate between a cell and its neighbors ($\langle V_{\text{area}} \rangle$) for all the cells of each region of the sepal at each floral stage imaged. The $\langle V_{\text{area}}$

$\langle V_{\text{area}} \rangle$ plots from Fig. 4F are reproduced here (wild type a-c and *vos1* a-d), for comparison to the wild-type tip and middle data. Flowers shown in panels C and D are the same as in panels A and B. The maturing tip cells of wild type sepals have lower $\langle V_{\text{area}} \rangle$ than the middle cells in the later stage wild-type sepals ($V_{\text{area}} = 6.54\% \pm 0.07\%$ for tip and $7.35\% \pm 0.12\%$ for middle; mean \pm SE, $p < 10^{-6}$ permutation test). Note that we normalized V_{area} by the growth rate, so that slower growth does not imply reduced variability between cells. V_{area} of the wild-type sepal tips is comparable to the highest level of V_{area} for *fish4* sepals.

The error bars represent the standard error. Scale bars represent 50 μm .

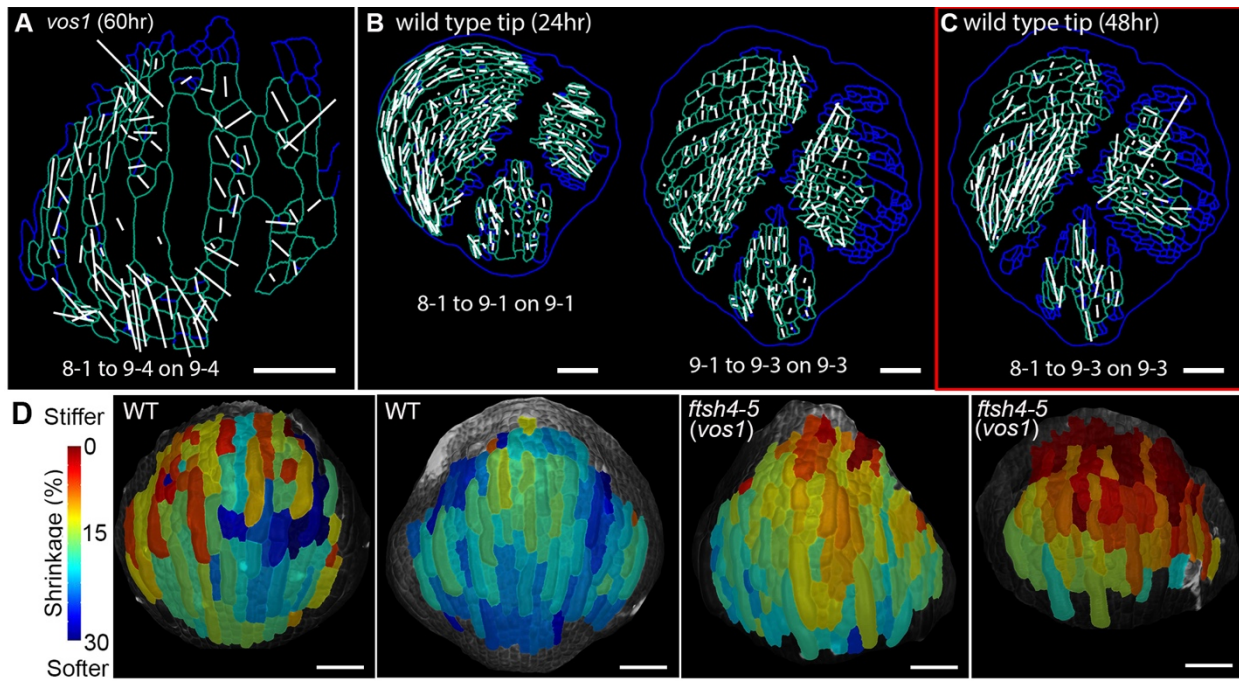


Figure S5 *vos1* sepal and wild-type sepal tip show less temporal averaging of variability in the cell growth directions and greater stiffness, related to Figure 5.

(A) The integrated growth directions of *vos1* sepal cells over 60 hours. The axes show the maximal growth directions (PDGs; white line) of the cells, with the length of the axes indicating the magnitude of the growth in that direction. The PDGs were mapped on the ending time point of the growth interval. Note that even after 60 hours the maximal growth directions are not well aligned.

(B) The PDGs of cells on the tip part of a wild-type sepal, calculated for each 24-hour interval of growth (stages at the bottom). Flower is the same as that shown in Figures S4A and S4C.

(C) The PDGs of the sepal tip cells calculated for the cumulative growth from 0 to 48 hours. The tip sepal cells show less temporal averaging of variability than cells in the middle of wild-type sepals, as the PDGs integrated for 48 hours are less aligned (compared with Figure 5B).

(D) Cell wall stiffness in wild type and *ftsh4-5 (vos1)* sepals at stages 8-9. When cells are placed in hypertonic solutions (high salt), water flows out of the cell decreasing the turgor pressure; the shrinkage of the cell is an indication of the cell wall elastic properties, with stiffer cells shrinking less. Cell wall stiffness is measured by calculating the change in area (% shrinkage) of the sepal epidermal cell region after osmotic treatment. Area shrinkage for each cell region is shown in heat maps on the segmented images. The lower the shrinkage the stiffer the cell wall. In the heat maps, the cells in red have low shrinkage / high stiffness and cells in blue have high shrinkage / low stiffness. Note that the sepal tips are stiffer than the middle part of the sepal.

Scale bars represent 50 μm.

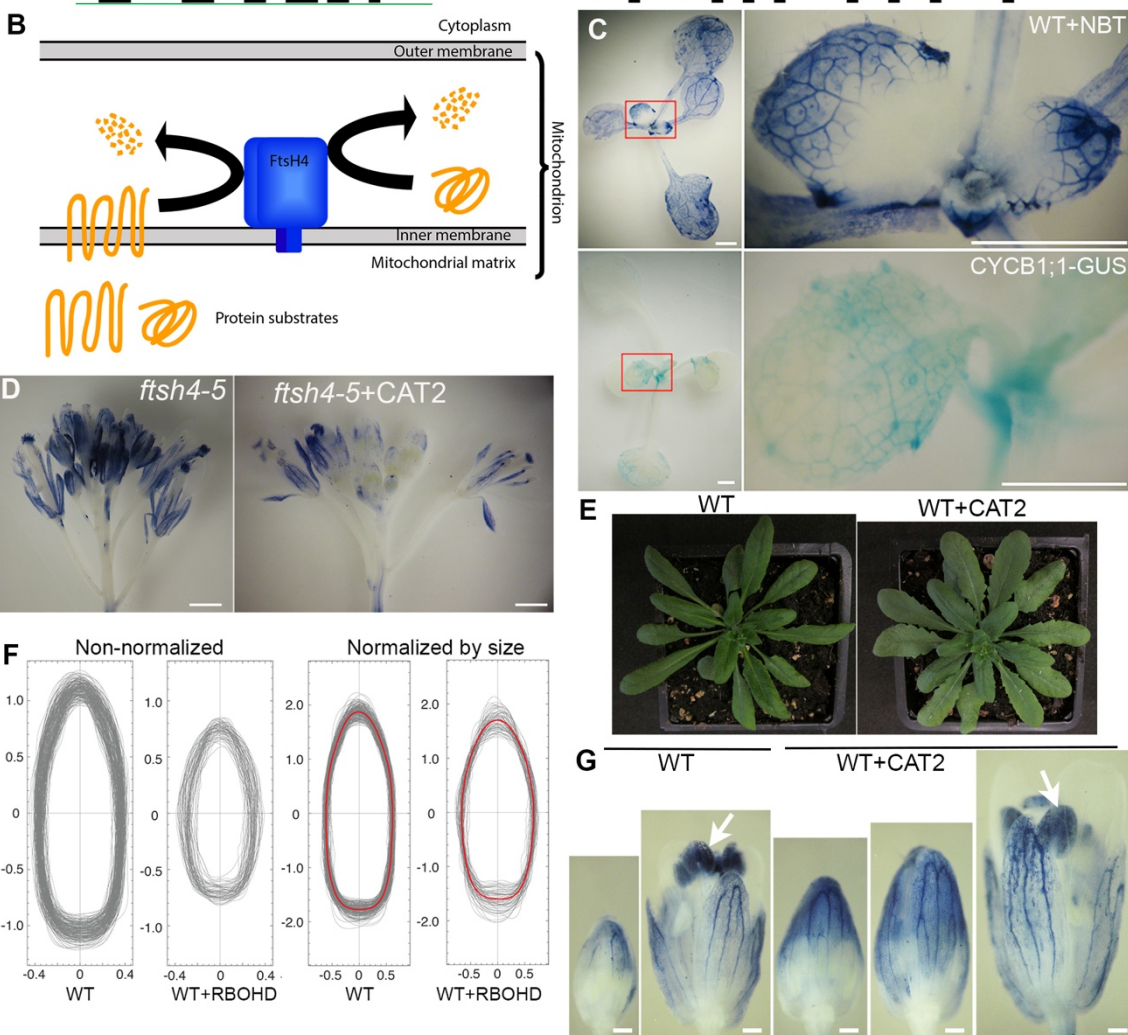
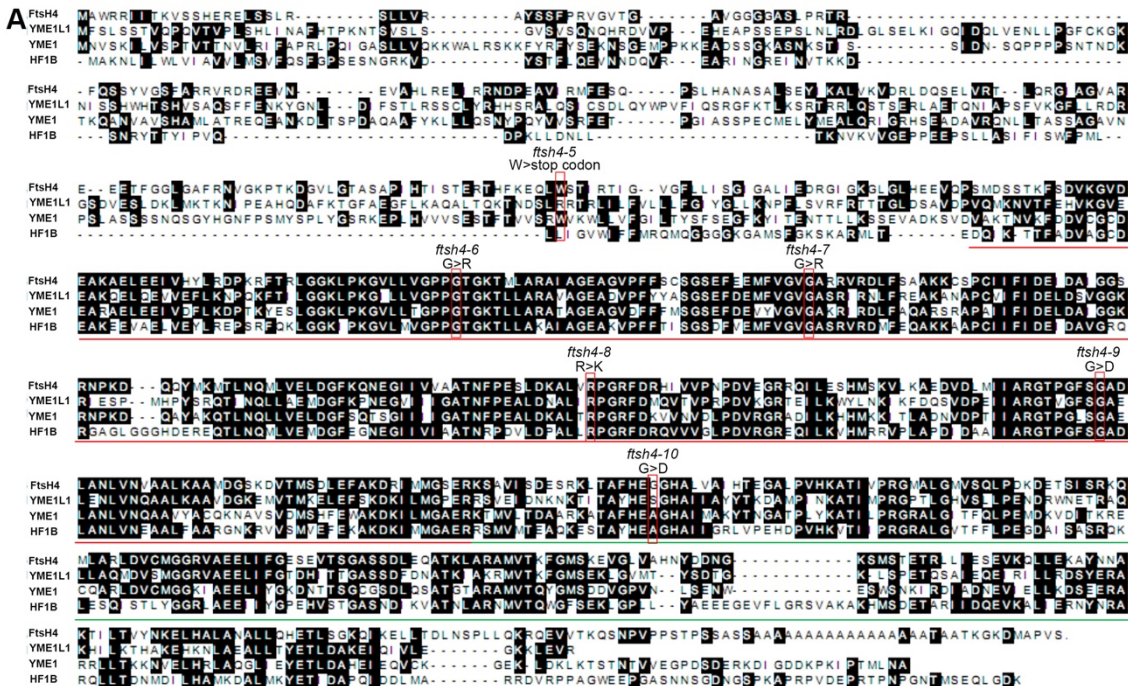


Figure S6 *FtsH4* mutations increases ROS and leads to variable sepals, related to Figure 6.

(A) Full-length protein alignment of FtsH4 homologs from *Arabidopsis* (FtsH4), human (*Homo sapiens*, YME1L1), yeast (*Saccharomyces cerevisiae*, YME1), and *E. coli* (*Escherichia coli*, HF1B). Sequences were aligned using the CLUSTAL W program. Conserved amino acid residues are shaded in black. The residues of the ATPase domain are highlighted in red, and the protease domain in green. The mutation sites for different *ftsh4* alleles isolated in this research are marked in red boxes, with the allele names and the amino acid changes labeled.

(B) The intra-mitochondrial localization and function of FtsH4 proteins.

(C) The superoxide distribution detected by NBT staining (upper panel) anticorrelates with cell division activity indicated by CYCB1;1-GUS expression (lower panel) in young wild-type leaves (Donnelly et al., 1999). Images on the right are magnifications of the red boxed regions in the left images. Similar to sepals, superoxide accumulates on the tip of the young leaves, where the cells have low cell division activity, and spreads toward the base as leaves grow. However, unlike sepals, the ROS accumulation occurred in relatively small leaves, long before growth terminated. Leaves undergo most of their growth through cell expansion after cell division stops (Gonzalez et al., 2012), suggesting this signal occurs at different times in organs with different morphologies.

(D) NBT staining for superoxide in flowers showing that overexpressing a catalase gene *CAT2* in *ftsh4-5* (*ftsh4-5*+*CAT2*) reduced superoxide level in the sepals, as the much lighter staining in *ftsh4-5*+*CAT2* sepals indicates.

(E) Wild-type plants overexpressing *CAT2* (WT+*CAT2*) have larger and more expanded leaf blades.

(F) Outlines (grey) of mature stage 14 sepals from WT and WT plants overexpressing a NADPH oxidase gene *RBOHD* (WT+*RBOHD*), showing decreased size and increased variation in shape. Outlines on the right have been normalized by sepal size and the median contours for each genotypes are shown in red revealing the difference in shape. WT data were reproduced from Fig. 1E for comparison.

(G) Wild-type plants overexpressing *CAT2* (WT+*CAT2*) have a similar but delayed superoxide gradient in sepals, which progresses downward as sepals mature. Although the overall pattern of progressive accumulation of superoxide from the tip to the base of the sepal is the same in WT and WT+*CAT2*, at a given sepal size, superoxide accumulation has progressed further down the WT sepal than the WT+*CAT2* sepal. In stage 14 flowers, stamens are strongly stained with NBT (arrows). To clearly visualize the superoxide accumulation pattern, flowers were stained for a longer time than flowers in D. Scale bars = 1 mm in C and D, 200 μ m in G.

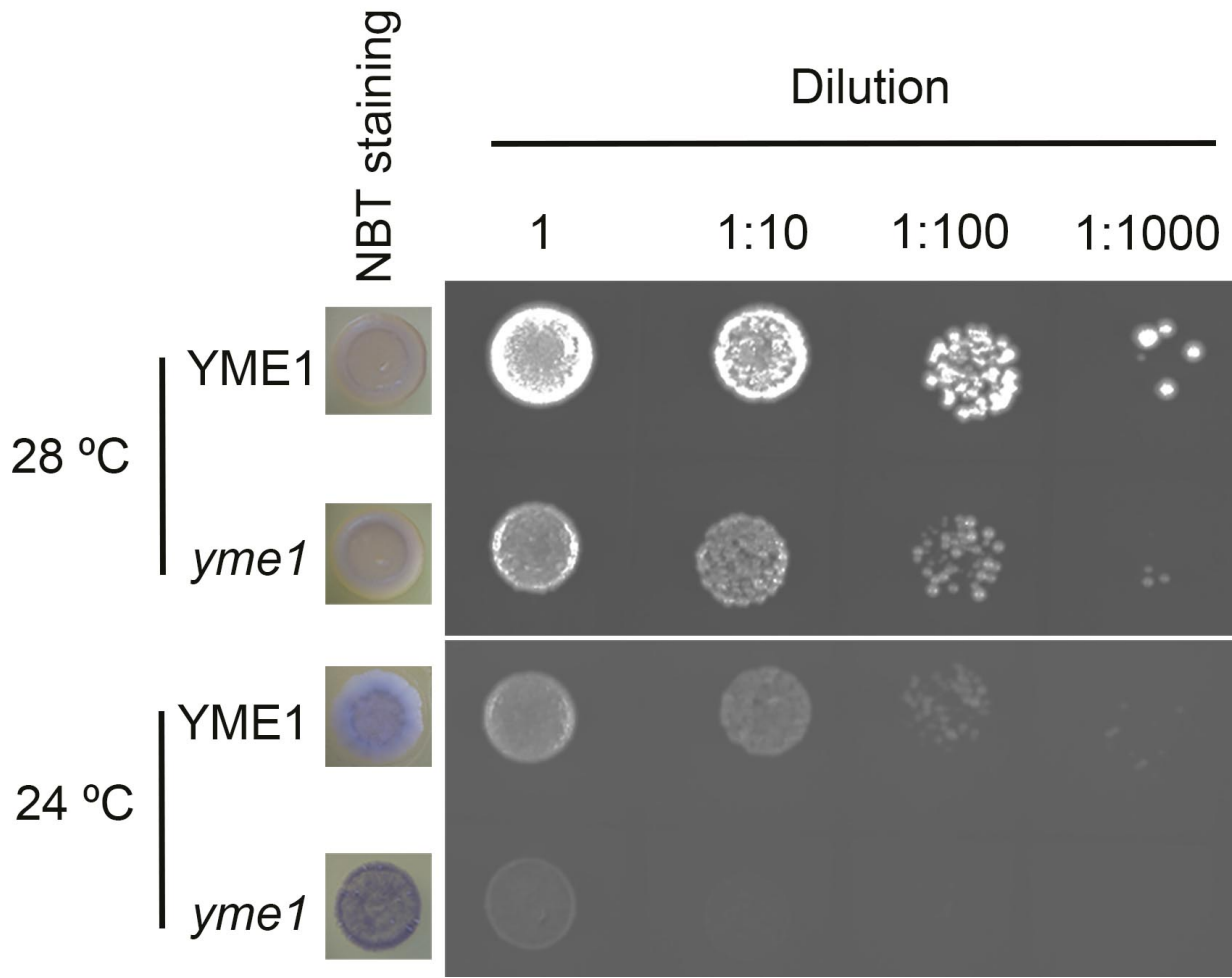


Figure S7 FtsH4 homolog YME1 affects growth rate and ROS production in yeast, related to Figure 6.

Growth assay of wild-type yeast (*YME1*) and *yme1* mutant (*yme1*) at optimal temperature 28°C or low temperature 24°C and NBT staining for superoxide level of yeasts growing at 24°C.

Upper row, yeasts growing at 28°C. Lower row, yeasts growing at 24°C. *yme1* mutants have similar growth rate and superoxide level when growing at 28°C. When growing at 24°C, *yme1* mutants produce higher superoxide and have lower proliferating activity.

Supplemental Movie Legends

Video S1: Non-variable (NV) model simulation, related to Figures 2 and 7

Video S2: Spatial variability (S) model simulation, related to Figure 2.

Video S3: Spatiotemporal variability (ST) model simulation, related to Figure 2.

Video S4: Spatiotemporal variability model with intermediate temporal variability (ST-0.1) simulation, related to Figures 2, S2, and 7.

In this model, mechanical properties are partially renewed: At each time point and at each vertex, mechanical properties are replaced by a weighted average of the properties at the previous step and of random properties following similar probability distribution functions. Here, the weight of the random modulus is 10% (ST-0.1) so that 90% of the previous properties are kept. This intermediate temporal variability is used in both the wild type-like and *ftsh4*-like models.

Video S5: Spatiotemporal variability model with low spatial variability (ST-L) simulation, related to Figure 2.

Video S6: Wild type-like (left) and *ftsh4*-like (right) model simulation, related to Figure 7.

Supplemental Data File Legend

Data File S1: Modeling and Analysis Code, related to Experimental Procedures

A zip file containing code for the model, multistep lineage tracking, sepal contour (outline) extraction and analysis, sepal shape analysis including the permutation test, and variability analysis.

Supplemental Experimental Procedures

Mutations and genotyping

Arabidopsis accession *Col-0* plants are used as wild type (WT) in this study. WT seeds were mutagenized with 0.3% ethyl methanesulfonate in 10 ml 0.02% Tween 20 for 24 hours. M2 plants (plants in the second generation after mutagenized plants were self-fertilized) were examined under a dissecting microscope for the variable sepal size phenotype. Mutants of interest were crossed with a Landsberg *erecta* accession plant to generate mapping populations. Mutations were isolated using standard map-based cloning (Lukowitz et al., 2000). The *ftsh4-5* mutation contains a G to A change at base 543 of the coding sequence of *FtsH4*, which generates a premature stop codon. The *ftsh4-5* mutation can be PCR-genotyped by amplifying with primers oLH168 and oLH169 (sequences listed in Primer Table) at 55°C annealing temperature, followed by digesting the product with NcoI to produce a 103-bp wild-type product or a 124-bp mutant product. *ftsh4-5* plants were backcrossed three times to wild-type *Col-0* plants prior to further analysis. Allelism tests were conducted between *ftsh4-5* and *ftsh4-6* (a G to A change at base 808 of the CDS, resulting in G to R change in amino acid residues), between *ftsh4-5* and *ftsh4-7* (a G to A change at base 910 of the CDS, resulting in G to R change in amino acid residues), and between *ftsh4-5* and *ftsh4-8* (a G to A change at base 1142 of the CDS, resulting in R to K change in amino acid residues). All alleles failed to complement *ftsh4-5*, establishing that the variable sepal size phenotype is due to the mutation in the *FtsH4* gene. Another two alleles, *ftsh4-9* (a G to A change at base 1289 of the CDS, resulting in G to D change in amino acid residues) and *ftsh4-10* (a G to A change at base 1463 of the CDS, resulting in G to D change in amino acid residues), were also isolated in the screen.

Flower stage

Flowers were staged according to (Smyth et al., 1990).

Sepal area measurements

Sepals dissected from stage 14 flowers were flattened between two slides and photographed on a black background using a dissecting microscope mounted with a camera. Custom Python programs (Data File S1) were used to extract each sepal's contour from the sepal photos and to measure sepal's area. Briefly, images were segmented using the watershed method. Contours were extracted and aligned along their longest axis determined by a principal component analysis of the contour points. Images and contours were smoothed on a scale of diameter 25 μ m. The data were sorted, analyzed and plotted in Microsoft Excel or the statistical software R.

Quantification of shape variability

The shape variability is studied by analyzing the sepal's contour points, $(x_1, y_1), \dots, (x_N, y_N)$ where N is the number of contour points, using Fourier methods (Data File S1). In order to remove the translational degree of freedom, the contours are first centered at the center of mass of the contour points, $(x_c, y_c) = (\frac{1}{N} \sum_{i=1}^N x_i, \frac{1}{N} \sum_{i=1}^N y_i)$. The radial distance $r(\theta)$ of the contour points from the center can then be obtained as a function of the polar angle θ . Since $\theta = 0$ is so far defined arbitrarily, we remove the rotational degree of freedom with the help of the polar Fourier transformation as $r(\theta) = r_0 + \sum_{n=1}^{n_{max}} c_n \cos(n(\theta + \phi_n))$. Here $r_0 = \frac{1}{2\pi} \int_0^{2\pi} r(\theta) d\theta$ is the average

radius of the contour, n_{\max} is chosen to be large enough such that the Fourier series well describe the fluctuations in $r(\theta)$, and ϕ_n specifies the angular phase of the n th Fourier mode. To fix the orientation of the contour, we choose the convention that $\phi_2 = 0$ for the second harmonic. The second harmonic is used to fixed the orientation since $r_{2nd}(\theta) = r_0 + \cos(2(\theta + \phi_2))$ represents a shape close to an ellipse, and setting $\phi_2 = 0$ implies that $\theta = 0$ is defined by the long axis of the ellipse-like shape. With the translation and orientation fixed, the non-normalized (in size) contours for each genotype are then plotted as shown in Figures S1D and S6F .

To further compare the contours independent of the sepal size, we consider the normalized contours with respect to the average radius, defined by $r_{norm}(\theta) = r(\theta)/r_0 = 1 + \sum_{n=1}^{n_{\max}} \frac{c_n}{r_0} \cos(n(\theta + \phi_n))$, with $\phi_2 = 0$. The normalized contours are plotted in Figures 1E and S6F in the main text. For each genotype, we also evaluate the “median” normalized contour, denoted by $\tilde{r}_{norm}(\theta)$, (red line in Figures 1E and S6F) that is defined by the median radius at each angle from the set of contours belonging to the same genotype. To quantify shape variability, we consider the squared deviation of a given contour $r_{norm,\alpha}(\theta)$ ($\alpha = 1, 2, \dots, N_{contour}$) from the median contour, $S_2 = \frac{1}{2\pi} \int_0^{2\pi} (r_{norm,\alpha}(\theta) - \tilde{r}_{norm}(\theta))^2 d\theta$. Here $N_{contour}$ is the number of sepal contours for the genotype under consideration. The median of S_2 from the set of contours of the same genotype provides us with a statistical measure of shape variability. The median, instead of the mean, is used in our analysis since it is relatively insensitive to the effects of outliers. We also note that the main reason to introduce Fourier analysis here is to remove the translation, orientation and size effects in the evaluation of shape variability. The box plots in Figures 1F and 6K give the S_2 of the different genotypes studied in this research.

Permutation test to check if two populations have the same statistics

We use the permutation test, which does not require the knowledge of the underlying distribution functions, to test if the statistics of two populations are the same (Data File S1). Suppose we have two populations, $\{x_1, \dots, x_M\}$ and $\{y_1, \dots, y_N\}$ with finite sizes M and N , respectively, and we want to test if these two populations have the same, e.g. median, with the presence of sampling errors. Let us denote the observed medians be \tilde{x} and \tilde{y} , respectively, and assume $\tilde{x} \geq \tilde{y}$ without loss of generality. In order to tell if the two medians are different, we consider the observed difference $\Delta = \tilde{x} - \tilde{y}$. One expects that if Δ is very large, it is more likely that the medians are different. To have a sense what value of Δ is big enough for us to draw a statistical conclusion, we compare the observed Δ with the cases when the medians are the same as follows: The two populations are joined to form a single population with size $M+N$, and the ordering of the elements is permuted. After the permutation, the medians of the first M elements and the last N elements, denoted by $\tilde{x}_{permute}$ and $\tilde{y}_{permute}$, respectively, are evaluated to obtain the permuted difference $\Delta_{permute} = \tilde{x}_{permute} - \tilde{y}_{permute}$. The above permutation is then carried out many times, e.g., 1000 times, to construct the distribution of $\Delta_{permute}$. Since $\tilde{x}_{permute}$ and $\tilde{y}_{permute}$ come out from the same population, the expectation value of $\Delta_{permute}$ should be zero and the distribution of $\Delta_{permute}$ represents the possible fluctuations in the value of $\Delta_{permute}$ due to finite sampling. Finally, the observed difference Δ is compared with the distribution of $\Delta_{permute}$ to obtain the one-sided p -value, which is defined as the percentage of $\Delta_{permute}$ having values larger than the observed Δ . A small p -value therefore implies that the observed Δ is large and it is more likely to have $\tilde{x} > \tilde{y}$. We declare that $\tilde{x} > \tilde{y}$ is statistical significant if the p -value is less than 5%.

SEM observation

Scanning electron microscopy was performed as described using a Leica 440 (Roeder et al., 2010).

Cell division activity analysis by GUS staining

Cell division activity in young leaves was assayed using the CYCB1-GUS transgenic line having the *CYCB1;1* promoter and the destruction box fused to the reporter *uidA* gene (Colón Carmona et al., 1999). GUS staining was performed as described (Sessions et al., 1999). In brief, seedlings were stained with staining solution (50 mM sodium phosphate buffer pH 7.0, 0.2% Triton-X-100, 10mM potassium ferrocyanide, 10mM potassium ferricyanide, 1mM X-gluc) overnight at 37 °C. The stained tissue was dehydrated and cleared with an ethanol series. GUS-stained seedlings were imaged with a digital camera mounted on a dissecting microscope.

Live imaging of sepal development

Live imaging of plants expressing pAR169 (pATML1::RCI2A-mCitrine) was conducted according to procedures in (Cunha et al., 2012; Roeder et al., 2010), except that plants were imaged every 12 hours. Three-dimensional optical stacks were collected with a Zeiss 710 confocal laser scanning microscope using a $\times 20$ water-immersion objective. The depth of z-sections was set to 0.5 μm for accurate curvature analysis. Samples were excited with an argon laser (488 nm), and data were collected in the yellow fluorescent protein (505 to 545 nm) channel. The resulting confocal stacks were converted from the LSM format to TIFF image stacks using FIJI (<http://fiji.sc/Fiji>) and imported into MorphoGraphX (Barbier de Reuille et al., 2015). The YFP stack was loaded into the software, and the stack was processed (Gaussian blur, edge detect, and fill holes) to obtain a sharp outline of the sepal abaxial surface. The surface was fit with a polygonal mesh using 5 μm cubes, and subsequently the mesh was subdivided and smoothed three times to $\sim 500,000$ vertices. YFP signal marking the plasma membrane was projected perpendicularly onto the surface from 4 to 8 μm depth within the stack, using the surface as measure 0 μm . Individual cells in the images were manually seeded and segmented using the watershed algorithm. For single growth intervals, cell lineage was defined manually by matching mother and daughter cell labels. For analyzing growth over several time points, progeny information between single time points was combined using 'Multi-step lineage tracking' (MSLT). MSLT is a script written in Python programming language which enables tracking cell clones over any permutation of time points in a time lapse imaging series in an automated way (Figures S3A-S3D; Data File S1). Heatmaps were generated to visualize the areal growth rate (defined as the cell lineage area at the second time point divided by cell area at the first time point). The values for each cell in the heatmaps were exported and analyzed with Microsoft Excel to calculate the mean of the logarithm of cell area, cellular area growth rate, and cell division rate for each sepal. The cell division rate for a sepal was calculated as the ratio of the number of cells that divided in the 12-hour growth interval to the total cell number at the beginning of that growth interval for the observed regions of the sepal.

Both wild-type and *vos1* flowers were developmentally staged by their flower width because flower width is minimally affected in *vos1* (Figures 1B, S1A, and S1B) (Smyth et al., 1990). Our SEM data (Figure 1B) showed that *vos1* sepal size irregularity appeared at relatively late stages, so flowers at stages 7 to 11 were used for imaging.

For mature sepal cell number and cell area measurements, sepals dissected from stage 14 flowers expressing pAR169 (*pATML1::RCI2A-mCitrine*) were imaged with a Zeiss 710 confocal laser scanning microscope using a $\times 20$ water-immersion objective. The stack images were

processed in MorphoGraphX to segment individual cells and calculate cell area, using the above mentioned procedures.

Detection and measurements of ROS

In situ detection of H₂O₂ and O₂⁻ were carried out as described previously (Dutilleul et al., 2003), with minor modifications. For H₂O₂ detection, inflorescences were vacuum-infiltrated (three cycles of 5 min) with 0.1% (w/v) DAB in 10 mM sodium phosphate buffer (pH 4)/Tween-20 (0.05% v/v) and incubated in the dark (covered with aluminum foil) at room temperature overnight. For O₂⁻ detection, inflorescences or seedlings were vacuum-infiltrated and incubated in 0.1% (w/v) NBT in 50 mM sodium phosphate buffer (pH > 6.8)/ 0.05% Tween-20 (v/v) for 90 min at room temperature in dark. After reaching the optimal staining state, stained samples were removed from the staining solution and cleared by boiling in acetic acid:glycerol:ethanol (1:1:3, v/v/v) solution. The clearing solution was replaced once after the boiling. After clearing, samples (sometimes individual flowers were detached from the inflorescence if necessary) were photographed against a white background using a dissecting microscope mounted with a camera.

Transgenic plants

The *YME1* gene, *CAT2* gene, and *APX1* gene full-length cDNA were first PCR amplified and cloned into pENTR/D-TOPO vectors (Invitrogen) as described in the manual, using primer pairs listed in Primer Table. The resultant vectors were LR recombined into the gateway vector pB7WG2 (Karimi et al., 2002) to generate three final constructs p35S::*YME1*, p35S::*CAT2* and p35S::*APX1*. All of the intermediate and final constructs were verified by sequencing. The three final constructs were individually transformed into *fish4-5* plants by *Agrobacterium*-mediated floral dipping. Seedlings about one week after germination were selected with 100 µg/mL Basta. Surviving plants were genotyped (primer sequences listed in Primer Table) and observed for sepal size phenotype.

For the overexpression of the *RBOHD* gene, the pOp/LhG4 inducible trans-activation system was used (Craft et al., 2005). The *RBOHD* gene full-length cDNA were first PCR amplified, using primer pairs listed in Primer Table, and cloned into a pBJ36-6xOPpro plasmid after the 6xOP promoter, resulting in plasmid pBJ36-6xOPpro:RBOHD. The 6xOPpro:RBOHD fragment from this plasmid was digested and cloned together with fragment 35Spro:GR-LhG4 (digested from the pBJ36-GR-LhG4) into the pMOA34 plasmid, to generate the pMOA34-6xOPpro:RBOHD-35Spro:GR-LhG4 construct. This final construct was transformed into wild-type plants by *Agrobacterium*-mediated floral dipping. Seeds were selected on 1/2MS medium with 50 µg/mL hygromycin. Surviving plants were transplanted to soil and genotyped (primer sequences listed in Primer Table). After the transgenic plants started bolting, the inflorescences were treated with a solution containing 5 µM dexamethasone (Sigma-Aldrich), 0.1% v/v ethanol and 0.01% v/v Silwet L-77, once every day for seven days. The flowers at stage 14 on these treated inflorescences were used for sepal size and shape analyses.

Primer Table: Primers used in this study.

Name	Primers	Description
oLH168	AGAAAGGACTCACTTAAAGAACAGCCATG	5' primer for <i>ftsh4-5</i> genotyping
oLH169	TCCTCTGCCTCGATAAGAGCTCC	3' primer for <i>ftsh4-5</i> genotyping
oLH266	CACCATGAACGTTCAAAAATACCTGTG	5' primer for amplifying <i>YME1</i> CDS and genotyping p35S::YME1
oLH267	TCATGCATTAAACATTGTAGGAA	3' primer for amplifying <i>YME1</i> CDS
oLH248	CACCATGGATCCTTACAAGTATCGTCCAG	5' primer for amplifying <i>CAT2</i> CDS
oLH249	TTAGATGCTTGGTCTCACGTTCAAG	3' primer for amplifying <i>CAT2</i> CDS
oLH233	CACCATGACGAAGAACTACCCAACCGTG	5' primer for amplifying <i>APX1</i> CDS
oLH234	CACACACACACAGAGCATACGTC	3' primer for amplifying <i>APX1</i> CDS
oLH275	TCTTCAACCTGTTGGACGTATG	5' primer for genotyping p35S::CAT2
oLH281	GATGGGCTTATCTGACAAAGACATT	5' primer for genotyping p35S::APX1
oAR424	GGAGAAAAATAGAGAGAGAGATAG	3' primer for genotyping p35S::YME1, p35S::CAT2 and p35S::APX1
oLH237	ATGAAAATGAGACGAGGCAATT	5' primer for amplifying <i>RBOHD</i> CDS
oLH238	CTAGAAGTTCTCTTGTGGAAGTC	3' primer for amplifying <i>RBOHD</i> CDS
oLH232	CACACACACACAGAGCATACGTC	5' primer for genotyping pMOA34-6xOPpro:RBOHD-35Spro:GR-LhG4
oAR315	CTACGTGTTCCGCTTCCTTAG	3' primer for genotyping pMOA34-6xOPpro:RBOHD-35Spro:GR-LhG4

Computational modeling

We built a continuous mechanical model for sepal morphogenesis (Data File S1), starting from a model previously developed for fission yeast (Bonazzi et al., 2014). Only surface cell walls are modeled, yielding a two-dimensional medium with a prescribed distribution of elastic modulus, E . Morphogenesis occurs by successive increments in area: the rest shape at step n is inflated by turgor pressure, P , leading to a new equilibrium shape, which is then used as a rest shape for the next step, $n+1$. At each step, the equilibrium configuration is found using the finite element method and the sepal is remeshed so as to keep a roughly constant mesh size. The model was implemented in Freefem++ (Hecht, 2012) and the results were analyzed using Python scripts. There are about 1500 epidermal cells in the *Arabidopsis* sepal (Roeder et al., 2010) and there are on average about 6 triangular elements per cell in the final model, which enables us to describe a cell with a complex shape and to allow some level of heterogeneity within one cell. In the present study, we accounted for three new ingredients: mechanical anisotropy, growth arrest front, and variable properties, as detailed hereafter.

Mechanical anisotropy was introduced to obtain a higher expansion rate along the y axis than the x axis, corresponding respectively to the proximo-distal and medio-lateral axes of the sepal. We thus used the generalized Hooke's law linking the stress tensor σ and the strain tensor ε through the elasticity matrix,

$$\begin{pmatrix} \sigma_{xx} \\ \sigma_{yy} \\ \sigma_{xy} \end{pmatrix} = \begin{pmatrix} A_1 & B & 0 \\ B & A_2 & 0 \\ 0 & 0 & C \end{pmatrix} \begin{pmatrix} \varepsilon_{xx} \\ \varepsilon_{yy} \\ \varepsilon_{xy} \end{pmatrix},$$

where $A_1 = (1 - \nu)E / ((1 + \nu)(1 - 2\nu))(1 + \alpha/2)$, $A_2 = (1 - \nu)E / ((1 + \nu)(1 - 2\nu))(1 - \alpha/2)$, $B = \beta\sqrt{A_1 A_2}$, $C = E / (1 + \nu)$, E being the reduced elastic modulus, ν the reduced

Poisson's ratio, α the mechanical anisotropy, and β a non-dimensional modulus ($\beta < 1$ for the elasticity matrix to be well-defined) (Landau and Lifshitz, 1986).

The starting configuration is always a semi-disk of radius 1.1. When the sepal reaches a length L , a front propagates proximally by a distance d per simulation step. The simulations are arrested when this front reaches the basis.

We considered variability of either the arrest front or the elastic modulus. In the former case, L is a random Gaussian variable of mean M_L and standard deviation S_L . In the latter, E is a random Gaussian variable, of mean M_E and standard deviation S_E , defined at each vertex and each time step; in order to avoid abnormally low stiffness, E is redrawn when it is smaller than T_E . In the case of pure spatiotemporal variability, the distribution of E is reset at each time step. In the case of pure spatial variability, the distribution of E is set in the initial configuration and then inherited throughout time: Following each remeshing, the value of modulus at a given vertex is interpolated from the previous mesh using the *adaptmesh* function of Freefem++.

In the intermediate case of partial renewal, the value of modulus E_n at step n is computed from the interpolated value E_{n-1} at step $n-1$, $E_n = (1-m) E_{n-1} + e$, where e is a random variable, of mean $M_E - (1-m) M_{n-1}$ and standard deviation $\sqrt{(S_E^2 - (1-m)^2 S_{n-1}^2)}$, where M_{n-1} and S_{n-1} are the mean and the standard deviation of the elastic modulus at step $n-1$ in the whole sepal. (E_n was also redrawn when smaller than T_E .) The renewal parameter m is such that $0 < m < 1$, $m = 0$ corresponding to no renewal and $m = 1$ to full renewal; $m=0.1$ (corresponding to 10% renewal) was used for the wild-type-like and the *ftsh4*-like models.

In the simulations shown here, we used $P = 0.5$ MPa, $E = 3.27$ MPa (estimated from AFM), $\nu = 0.48$, $\alpha = 0.2$, $\beta = 0.5$, $L = 3$, $d = 0.05$. The parameters for the random variables were $M_L = 3$ or 2.7, $S_L = 0.05$ or 0.5, $M_E = 3.27$ MPa, $S_E = 2.7$ MPa, $T_E = 0.1$ Mpa. The size of the mesh was 1/1.5, 1/5, and 1/3.5 corresponding to high (ST), low (ST-L), and *ftsh4*-like local variability, respectively. In addition, we explored a range of other values and found the same qualitative results.

Atomic force microscopy (AFM)

Stage 10 flowers were dissected off the stem and then put in a Petri dish containing solid growth medium as described (Fernandez et al., 2010). The flowers were oriented with abaxial sepals facing upward and covered with a water drop for measurements. Atomic force microscopy was performed as described in (Milani et al., 2013), with minor modifications. We used a JPK Nanowizard AFM with an extended stage enabling a vertical range of 100 μ m, which was required because of the bumpiness of the sepal surface. The cantilevers (SCANASYST-AIR, Bruker Inc.) had a nominal spring constant of 7N/m and a pyramid-shaped tip (tip angle 18°, nominal radius 2 nm). Each cantilever was calibrated by using indentation on sapphire and thermal tune, in water. Areas of about 100 μ m x 100 μ m in the center of the sepal were first scanned to obtain sample topography, then approach and retraction were performed on a square grid of 20x20 equally separated points, with two measurements at each point, yielding 800 curves per sepal. Approach and retract velocity was 5 μ m/s. Maximal depths ranged from 100 to 200 nm, in order to obtain curves that are mostly sensitive to cell wall mechanics. Force curves were fitted to the Hertz-Sneddon equation as in (Milani et al., 2013); fits with coefficient of determination smaller than 0.95 (about 20% of the

data) were discarded. We thus obtained effective elastic moduli that quantify cell wall mechanics around each point of the grid.

Osmotic treatments measuring sepal stiffness

All flowers except for one of stage 8-9 were dissected off the inflorescence. The sample was incubated in water containing 0.1% PPM (Plant Cell Technology) for 1-2 hours and stained in 0.1% Propidium Iodide solution (Sigma-Aldrich) for 15 minutes. The sample was immobilized in $\frac{1}{2}$ MS medium in such a way that the end of the stem was stuck in the medium and the flower remained above the surface of the medium covered in water and the first confocal stack was taken. The water was then removed and the sample was incubated in NaCl (Roth) solution for 30 minutes. Confocal stacks were taken directly before and after NaCl treatment.

The concentration of osmolyte in which epidermal cell plasmolysis can be observed was determined by conducting the osmotic treatment procedure on *Col-0* flowers in NaCl concentrations ranging from 0.2 M to 1 M. PI was used to visualize the cell wall and pUBQ10::myrYFP marker donated by Raymond Wightman was used to visualize the plasma membrane. In this marker line YFP is N-terminally modified with a short myristoylated and probably acetylated peptide. The optimal NaCl concentration for which plasma membrane was visibly detached from the cell wall while maintaining good image quality was 0.4 M for both *Col-0* and *ftsh4* sepals.

For confocal imaging SP8 microscope with water immersion long working distance objective (HCX APO 40x/0.8, Leica) was used. Images were collected at 605-664 nm for PI (excitation at 524 nm, argon laser) and 520-550 nm for YFP (excitation at 488 nm, argon laser).

Images from before and after the osmotic treatment were segmented in MorphoGraphX. Giant cells were segmented individually while small cells were clustered in groups which shape roughly resembled the shape of giant cells. Change in cell area (% shrinkage) was calculated and displayed on the segmented images as heat map. When cells are placed in hypertonic solutions (high salt), water flows out of the cell decreasing the turgor pressure; the shrinkage of the cell is an indication of the cell wall elastic properties, with stiffer cells shrinking less.

Analysis of spatiotemporal variability in the growth of cell area

The growth of cell area was based on the quantification of area in MorphographX (Barbier de Reuille et al., 2015). In this analysis (Data File S1), we used the consecutive areas of the cells with same lineage. If the mother cell divided during the time interval, the areas of all daughter cells were summed in order to calculate the corresponding areal growth rate. The areas of the parent cell and all the daughter cells were denoted by A_x and A_y , respectively. Then, the areal growth rate was defined as $AGR = (A_y/A_x)/\Delta t$ where Δt is the time interval of the consecutive time frames. In order to calculate the local spatial variability in the areal growth rate among neighboring cells, we defined the areal growth rate for the cell of interest (labelled f) as $AGR(f)$ and for neighboring cells surrounding cell f as $AGR(i)$ where $i = 1, 2, \dots, N$ (N is the number of neighbors of cell f). Then, the difference of the areal growth rates among neighboring cells was defined as $V_{area} =$

$\frac{1}{N} \sum_{i=1}^N \frac{|AGR(f) - AGR(i)|}{|AGR(f) + AGR(i)|}$. The areal growth rates with cumulative probability $p(V_{\text{area}}) > 0.95$ were taken as outliers.

In order to calculate the temporal variation of the areal growth rate, we defined the areal growth rate for the cell of interest at the current time frame as $AGR^{(t)}$ and the areal growth rate for the same cell at the next time frame as $AGR^{(t+\Delta t)}$. If the cell of interest has divided into m cells, we obtain m different quantitites of the type $AGR^{(t+\Delta t)}$. The temporal variation of the areal growth rate for the same cell lineages between consecutive growth intervals was then defined as $D_{\text{area}} = \frac{|AGR^{(t)} - AGR^{(t+\Delta t)}|}{|AGR^{(t)} + AGR^{(t+\Delta t)}|}$. In this case, the areal growth rates with cumulative probability $p(D_{\text{area}}) > 0.95$ were taken as outliers.

Accession Numbers

FtsH4/VOS1, AT2G26140; *CAT2*, AT4G35090; *APX1*, AT1G07890; *RBOHD*, AT5G47910; *FtsH3*, AT2G29080; *FtsH10*, AT1G07510; *FtsH11*, AT5G53170; *YME1L1*, AJ132637; *YME1*, DQ333030; *HF1B*, NP_417645

Supplemental References

Barbier de Reuille, P., Routier-Kierzkowska, A.L., Kierzkowski, D., Bassel, G.W., Schüpbach, T., Tauriello, G., Bajpai, N., Strauss, S., Weber, A., Kiss, A., et al. (2015). MorphoGraphX: A platform for quantifying morphogenesis in 4D. *eLife* 4, e05864.

Bonazzi, D., Julien, J.-D., Romao, M., Seddiki, R., Piel, M., Boudaoud, A., and Minc, N. (2014). Symmetry breaking in spore germination relies on an interplay between polar cap stability and spore wall mechanics. *Dev Cell* 28, 534–546.

Colón Carmona, A., You, R., Haimovitch Gal, T., and Doerner, P. (1999). Spatio-temporal analysis of mitotic activity with a labile cyclin–GUS fusion protein. *Plant J* 20, 503–508.

Craft, J., Samalova, M., Baroux, C., Townley, H., Martinez, A., Jepson, I., Tsiantis, M., and Moore, I. (2005). New pOp/LhG4 vectors for stringent glucocorticoid-dependent transgene expression in *Arabidopsis*. *Plant J* 41, 899–918.

Cunha, A., Tarr, P.T., Roeder, A.H.K., Altinok, A., Mjolsness, E., and Meyerowitz, E.M. (2012). Computational analysis of live cell images of the *Arabidopsis thaliana* plant. *Methods Cell Biol.* 110, 285–323.

Donnelly, P.M., Bonetta, D., Tsukaya, H., Dengler, R.E., and Dengler, N.G. (1999). Cell cycling and cell enlargement in developing leaves of *Arabidopsis*. *Dev Biol* 215, 407–419.

Fernandez, R., Das, P., Mirabet, V., Moscardi, E., Traas, J., Verdeil, J.-L., Malandain, G., and Godin, C. (2010). Imaging plant growth in 4D: robust tissue reconstruction and lineageing at cell resolution. *Nat Methods* 7, 547–553.

Gonzalez, N., Vanhaeren, H., and Inzé, D. (2012). Leaf size control: complex coordination of cell division and expansion. *Trends Plant Sci* 17, 332–340.

- Hecht, F. (2012). New development in FreeFem++. *J Numer Math* 20, 251–266.
- Karimi, M., Inzé, D., and Depicker, A. (2002). GATEWAY™ vectors for *Agrobacterium*-mediated plant transformation. *Trends Plant Sci* 7, 193–195.
- Landau, L.D., and Lifshitz, E.M. (1986). Theory of Elasticity (Oxford: Pergamon Press).
- Lukowitz, W., Gillmor, C.S., and Scheible, W.R. (2000). Positional cloning in *Arabidopsis*. Why it feels good to have a genome initiative working for you. *Plant Phys* 123, 795–805.
- Milani, P., Braybrook, S.A., and Boudaoud, A. (2013). Shrinking the hammer: micromechanical approaches to morphogenesis. *J Exp Bot* 64, 4651–4662.
- Roeder, A.H.K., Chickarmane, V., Cunha, A., Obara, B., Manjunath, B.S., and Meyerowitz, E.M. (2010). Variability in the control of cell division underlies sepal epidermal patterning in *Arabidopsis thaliana*. *PLoS Biol* 8, e1000367.
- Sessions, A.A., Weigel, D.D., and Yanofsky, M.F.M. (1999). The *Arabidopsis thaliana* MERISTEM LAYER 1 promoter specifies epidermal expression in meristems and young primordia. *Plant J* 20, 259–263.
- Smyth, D.R., Bowman, J.L., and Meyerowitz, E.M. (1990). Early flower development in *Arabidopsis*. *Plant Cell* 2, 755–767.